Available online at www.sciencedirect.com
ScienceDirect
Journal of Computational Physics 221 (2007) 666–692
JOURNAL OF COMPUTATIONAL PHYSICS
www.elsevier.com/locate/jcp

Numerical simulation of fully nonlinear interaction between steep waves and 2D floating bodies using the QALE-FEM method

S. Yan, Q.W. Ma *

School of Engineering and Mathematical Sciences, City University, Northampton Square, London EC1V 0HB, UK

Received 15 November 2005; received in revised form 9 June 2006; accepted 26 June 2006
Available online 17 August 2006

Abstract

This paper extends the QALE-FEM (quasi arbitrary Lagrangian–Eulerian finite element method) based on a fully nonlinear potential theory, which was recently developed by the authors [Q.W. Ma, S. Yan, Quasi ALE finite element method for nonlinear water waves, J. Comput. Phys, 212 (2006) 52–72; S. Yan, Q.W. Ma, Application of QALE-FEM to the interaction between nonlinear water waves and periodic bars on the bottom, in: 20th International Workshop on Water Waves and Floating Bodies, Norway, 2005], to deal with the fully nonlinear interaction between steep waves and 2D floating bodies. In the QALE-FEM method, complex unstructured mesh is generated only once at the beginning of calculation and is moved to conform to the motion of boundaries at other time steps, avoiding the necessity of high cost remeshing. In order to tackle challenges associated with floating bodies, several new numerical techniques are developed in this paper. These include the technique for moving mesh near and on body surfaces, the scheme for estimating the velocities and accelerations of bodies as well as the forces on them, the method for evaluating the fluid velocity on the surface of bodies and the technique for shortening the transient period. Using the developed techniques and methods, various cases associated with the nonlinear interaction between waves and floating bodies are numerically simulated. For some cases, the numerical results are compared with experimental data available in the public domain and good agreement is achieved.

Keywords: QALE-FEM; Nonlinear water waves; Spring analogy method; Iterative procedure; 2D floating bodies

1. Introduction

With operations in the oil and gas industry moving to deeper water, offshore structures are more likely to be exposed to very harsh environments and extremely steep waves and therefore undergo large motions. As a result, there is an increasing interest in numerically simulating nonlinear water waves and their interaction with floating structures. Two classes of theoretical models for cases with finite water depth are in common

* Corresponding author. Tel.: +44 20 7040 8159; fax: +44 20 7040 8566.
E-mail address: q.ma@city.ac.uk (Q.W. Ma).

0021-9991/$ - see front matter
doi:10.1016/j.jcp.2006.06.046

use for numerical simulations. One is based on general flow theory and the other is based on potential theory. In the first class of models, the Navier–Stokes and continuity equations together with proper boundary conditions are solved; while in the second class, the Laplace equation with fully nonlinear boundary conditions are dealt with. For brevity, the first class of models will be called NS Model and the second called FNPT (representing fully nonlinear potential theory) Model in the paper.

In the community of researchers who use the NS Model, three formulations have been suggested: Eulerian, Lagrangian and arbitrary Lagrangian–Eulerian (ALE) formulations. Various numerical methods, such as finite element, finite volume and finite difference methods, have been adopted to solve the Navier–Stokes and continuity equations together with one of three formulations. However, whichever formulation is used, solving the NS equations is always a time consuming task. As a result, the FNPT Model has been employed in many publications for problems associated with nonlinear water waves and their interaction with structures. In this model, viscosity is ignored. The governing equations are dramatically simplified and therefore need much less computational resources to be solved than in the NS Model. Comparison with experimental data [3–6] has shown that the results obtained by using this model are accurate enough if breaking waves do not occur and/or if structures involved are large. Therefore, the FNPT Model, instead of the NS Model, should be preferred if a case considered falls in this category.

The problems formulated by FNPT model are usually solved by a time marching procedure suggested by Longuet-Higgins and Cokelet [7]. In this procedure, the key task is to solve the boundary value problem by using an efficient numerical method, such as the boundary element method (BEM) or the finite element method (FEM). The BEM has been attempted by many researchers, such as Vinje and Brevig [8], Lin et al. [9], Wang et al. [10], Kashiwagi [11], Cao et al. [12], Celebi et al. [13], Grilli et al. [14] and Kim et al. [15]. The FEM has been developed by Wu and Eatock Taylor [16,17] for two-dimensional cases and by Ma et al. [5,6] and Ma [18] for three-dimensional cases. All the above publications are concerned with problems either about fixed bodies or those with a prescribed motion. Until now, the publications about the interaction between fully nonlinear waves and free-response bodies are still very limited. Beck and Schultz [19] made nonlinear computation of wave loads and motions of freely rectangular barge in incident waves. Tanizawa [20], Tanizawa and Minami [21] and Tanizawa et al. [22] simulated 2D freely barge-type floating body, followed by Koo [23] and Koo and Kim [24]. Kashiwagi and Momoda [25] and Kashiwagi [26] investigated wave-induced motions of 2D complicated-shape floating body. All of them used the BEMs. Recently, Wu and Hu modelled the interaction between waves and a 3D cylindrical FPSO-like structure [27] in which the FEM was applied.

Both the BEM and the FEM have been proved efficient but the later require less memory and is therefore computationally more efficient for fully nonlinear wave–body problems, as indicated by Ma et al. [5] and Wu and Eatock Taylor [16]. A disadvantage of the FEM, however, is that a complex unstructured mesh is necessary for complicated geometries to achieve accurate results, which may need to be regenerated at every time step to follow the motion of waves and bodies. Repeatedly regenerating such a mesh may take a major part of CPU time and so makes the overall simulation very slow. To reduce the CPU time spent on updating the mesh, a simple structured mesh was used in [5,6,16–18]. Wu and Hu [27] recently developed a hybrid mesh for the same purpose but it was restricted only to cylindrical structures without rotational motions because of the limitation of the mesh structure. The problem associated with mesh has become a bottleneck in the development of efficient methods dealing with the interaction between water waves and freely floating bodies. To overcome the difficulty, Ma and Yan [1,2] have recently invented a QALE-FEM (quasi arbitrary Lagrangian–Eulerian finite element method). The main idea of this method is that the complex unstructured mesh is generated only once at the beginning of calculation and is moved at other time steps to conform to motions of boundaries. This feature allows one to use an unstructured mesh with any degree of complexity without the need of regenerating it at every time step. Ma and Yan [1] compared the QALE-FEM with conventional FEM in terms of computational efficiency and accuracy in the cases with periodic bars on the seabed. They concluded that the QALE-FEM may require less than 15% of the CPU time required by the conventional FEM at the same accuracy level. However, they applied the new method only to cases without floating bodies.

In this paper, the QALE-FEM is extended to deal with problems involving 2D freely floating bodies. In order to tackle the challenges associated with floating bodies, several new numerical techniques are developed. These include a technique for moving the mesh near and on the body surface, a scheme for estimating the velocities and accelerations of bodies as well as the forces on them, a method for evaluating the fluid velocity

on the surface of bodies and a technique for shortening the transient period. The last technique is beneficial to investigations of response amplitude operators (RAOs) of floating bodies in waves, which require reaching a steady state (all motions being periodic with roughly constant amplitudes) as soon as possible in order to save CPU time. Using these developed techniques, various cases associated with the nonlinear interaction between waves and floating bodies are numerically simulated. For some cases, the numerical results are compared with experimental data available in the public domain and good agreement is achieved.

2. Mathematical model and numerical method

In this paper, waves are generated by a piston-like wavemaker in a tank as shown in Fig. 1. The wavemaker is mounted at the left end and a damping zone with a Sommerfeld condition (see [5,18] for details) is applied at the right end of the tank in order to suppress the reflection. A Cartesian coordinate system is used with the oxy plane on the mean free surface and with the z-axis being positive upwards. A floating body is placed at $x = 0$ initially and moored to the bed or walls of the tank.

2.1. FNPT model for fluid

Similar to the usual formulation for the FNPT Model, the velocity potential (ϕ) satisfies Laplace's equation,

$$\nabla^2\phi = 0 \tag{1}$$

in fluid domain. On the free surface $z = \zeta(x, y, t)$, the velocity potential satisfies the kinematic and dynamic conditions in the following Lagrangian form:

$$\frac{Dx}{Dt} = \frac{\partial\phi}{\partial x}, \quad \frac{Dy}{Dt} = \frac{\partial\phi}{\partial y}, \quad \frac{Dz}{Dt} = \frac{\partial\phi}{\partial z}, \tag{2}$$

$$\frac{D\phi}{Dt} = -gz + \frac{1}{2}|\nabla\phi|^2, \tag{3}$$

where $\frac{D}{Dt}$ is the substantial (or total time) derivative following fluid particles and g is the gravitational acceleration. In Eq. (3), the atmospheric pressure has been taken as zero. On all rigid boundaries, such as the wavemaker and the floating body, the velocity potential satisfy

$$\frac{\partial\phi}{\partial n} = \vec{n} \cdot \vec{U}(t), \tag{4}$$

where $\vec{U}(t)$ and $\vec{n}$ are the velocity and the unit normal vector of the rigid boundaries, respectively. The positive direction of the normal vector points to the outside of the fluid domain.

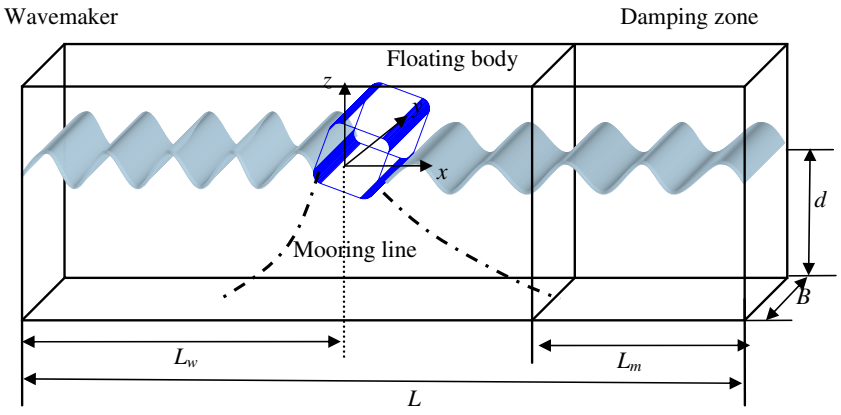

Fig. 1. Sketch of fluid domain.

2.2. Motion equations of a floating body

The displacements, velocities and accelerations of a floating body are governed (see e.g. [18,28]) by

$$[M]\vec{\dot{U}}_c = \vec{F}, \tag{5a}$$

$$[I]\vec{\dot{\Omega}} + \vec{\Omega} \times [I]\vec{\Omega} = \vec{N}, \tag{5b}$$

$$\frac{d\vec{S}}{dt} = \vec{U}_c, \tag{6a}$$

$$[B]\frac{d\vec{\theta}}{dt} = \vec{\Omega}, \tag{6b}$$

where $\vec{F}$ and $\vec{N}$ are the force and moment acting on the floating body; $\vec{U}_c$ and $\vec{\dot{U}}_c$ the translational velocity and acceleration of its gravitational centre; $\vec{\Omega}$ and $\vec{\dot{\Omega}}$ its angular velocity and acceleration; $\vec{\theta}(\alpha, \beta, \gamma)$ the Euler angles; $\vec{S}$ the translational displacements. In Eqs. (5) and (6), $[M]$ and $[I]$ are mass and inertia matrixes, respectively; and $[B]$ is the matrix formed by Euler angles and defined as,

$$[B] = \begin{bmatrix} \cos\beta\cos\gamma & \sin\gamma & 0 \\ -\cos\beta\sin\gamma & \cos\gamma & 0 \\ \sin\beta & 0 & 1 \end{bmatrix}. \tag{7}$$

In 2D cases, $\vec{\Omega} \times [I]\vec{\Omega} = 0$, $\alpha = 0$, $\gamma = 0$, Eqs. (5b) and (6b) can be rewritten as

$$[I]\vec{\dot{\Omega}} = \vec{N}, \tag{8}$$

$$\frac{d\vec{\theta}}{dt} = \vec{\Omega}. \tag{9}$$

Once $\vec{U}_c$ and $\vec{\Omega}$ are known, the velocity at a point on the body is determined by

$$\vec{U} = \vec{U}_c + \vec{r}_b \times \vec{\Omega}, \tag{10}$$

where r_b is the position vector relative to the gravitational centre.

2.3. Force calculation

The force ($\vec{F}$) and moment ($\vec{N}$) acting on a body in Eqs. (5) and (6) can be evaluated by,

$$\vec{F} = -\rho \int\int_{S_b} \left(\frac{\partial\phi}{\partial t} + \frac{1}{2}|\nabla\phi|^2 + gz\right)\vec{n}\, ds + \vec{f}_m, \tag{11}$$

$$\vec{N} = -\rho \int\int_{S_b} \left(\frac{\partial\phi}{\partial t} + \frac{1}{2}|\nabla\phi|^2 + gz\right)\vec{r}_b \times \vec{n}\, ds + \vec{N}_m, \tag{12}$$

where S_b denotes the wetted body surface. $\vec{f}_m$ and $\vec{N}_m$ are forces and moments due to mooring lines, respectively. Because this paper focuses on the wave–body interaction, the mooring lines are approximated by using linear springs, i.e.,

$$\vec{f}_m = k_m\vec{S}_m, \tag{13a}$$

$$\vec{N}_m = \vec{r}_m \times \vec{f}_m \tag{13b}$$

in which k_m is the spring stiffness, $\vec{S}_m$ is the displacement of the mooring point, $\vec{r}_m$ is the position vector of the mooring point relative to the gravitational centre.

As can be seen, the time derivative of the velocity potential ($\partial\phi/\partial t$) is required and is critical for accurately calculating forces and moments. A simplest way to calculate $\partial\phi/\partial t$ is to use a backward finite difference scheme:

$$\left(\frac{\partial\phi}{\partial t}\right)^n = \frac{\phi^n - \phi^{n-1}}{\Delta t}, \tag{14}$$

where Δt is the time step and the superscript n denotes nth time step. As is well known, however, the scheme may suffer from a problem of the saw-tooth instabilities [29]. An alternative approach is to find $\partial\phi/\partial t$ by solving a similar boundary value problem to that for ϕ defined in Eqs. (1)–(4) (see for example [5,6,16–18]). The boundary value problem for $\partial\phi/\partial t$ is defined by,

$$\nabla^2\left(\frac{\partial\phi}{\partial t}\right) = 0 \tag{15}$$

in the fluid domain. On the free surface $z = \zeta(x, y, t)$, it is given by

$$\frac{\partial\phi}{\partial t} = -g\zeta - \frac{1}{2}|\nabla\phi|^2. \tag{16}$$

On all rigid boundaries, it satisfies

$$\frac{\partial}{\partial n}\left(\frac{\partial\phi}{\partial t}\right) = [\vec{\dot{U}}_c + \vec{\dot{\Omega}} \times \vec{r}_b] \cdot \vec{n} - \vec{U}_c \cdot \frac{\partial\nabla\phi}{\partial n} + \vec{\Omega} \cdot \frac{\partial}{\partial\vec{n}}[\vec{r}_b \times (\vec{U}_c - \nabla\phi)]. \tag{17}$$

It should be noted here that there is a difficult with solving Eqs. (15)–(17). As can be seen from Eq. (17), the accelerations $\vec{\dot{U}}_c$ and $\vec{\dot{\Omega}}$ should be known when solving the boundary value problem for $\partial\phi/\partial t$. However, in cases involving a free-response floating body, they are evaluated by Eqs. (5) and (6), which depends on the force and moment given in Eqs. (11) and (12). In turn, to find the force and moment, one needs $\partial\phi/\partial t$. The scheme to overcome this difficulty will be detailed in Section 5.

2.4. FEM formulation

The full details about the FEM formulation have been discussed in our previous publications, for example [1,5,18]. They will not be repeated here. Only summary of the formulation is given below.

The problem described by Eqs. (1)–(4) will be solved by using a time step marching procedure. At each time step, the free surface and the potential values on it as well as velocities on all rigid boundaries are known. Thus, the boundary condition for the potential on the free surface can be replaced by a Dirichlet condition:

$$\phi = f_p, \tag{18}$$

where f_p is the potential values on the free surface, which can be estimated by using Eq. (3) and a time integration scheme with second order accuracy. Therefore, the unknown velocity potential in the fluid domain can be found by solving a mixed boundary value problem which is defined by Eqs. (1), (4) and (18). To do so, the fluid domain is discretised into a set of small tetrahedral elements and the velocity potential is expressed in terms of a linear shape function, $N_J(x, y, z)$:

$$\phi = \sum_J \phi_J N_J(x, y, z), \tag{19}$$

where ϕ_J is the velocity potential at node J. Using the Galerkin method, the Laplace equation and the boundary conditions are discretised as follows:

$$\int\int\int_{\forall} \nabla N_I \cdot \sum_{\substack{J \\ J\notin S_P}} \phi_J \nabla N_J \, d\forall = \int\int_{S_n} N_I f_n \, dS - \int\int\int_{\forall} \nabla N_I \cdot \sum_{\substack{J \\ J\in S_P}} (f_p)_J \nabla N_J \, d\forall, \tag{20}$$

where S_P represents the Dirichlet boundary on which the velocity potential f_p is known and S_n represents the Numann boundary on which the normal derivative of the velocity potential f_n is known. Eq. (20) can further be written in the matrix form:

$$[A]\{\phi\} = \{B\}, \tag{21}$$

where

$$\{\phi\} = [\phi_1, \phi_2, \phi_3, \ldots, \phi_I, \ldots]^{\mathrm{T}} \quad (I \notin S_P), \tag{22a}$$

$$A_{IJ} = \int\int_{\forall}\int \nabla N_I \cdot \nabla N_J \, \mathrm{d}\forall \quad (I \notin S_P, J \notin S_P), \tag{22b}$$

$$B_I = \int\int_{S_n} N_I f_{\mathrm{n}} \, \mathrm{d}S - \int\int_{\forall}\int \nabla N_I \cdot \sum_{J \in S_P} (f_p)_J \nabla N_J \, \mathrm{d}\forall \quad (I \notin S_P). \tag{22c}$$

The algebraic equation (21) is solved by using a conjugate gradient iterative method with SSOR pre-conditioner and optimised parameters [18]. The problem about $\partial\phi/\partial t$ described in Eqs. (15)–(17) is also solved by using the above method with ϕ and the boundary conditions for it are replaced by $\partial\phi/\partial t$ and corresponding boundary conditions for $\partial\phi/\partial t$.

3. Summary of QALE-FEM method

As indicated in Section 1, the QALE-FEM developed in [1] will be extended in this paper to deal with problems with 2D floating bodies. In this section, the key elements of the QALE-FEM in [1] are summarised before presenting new developments of this paper.

3.1. Scheme for moving mesh

The main idea of the QALE-FEM is that the complex unstructured mesh is generated only once at the beginning of calculation and is moved at other time steps to conform to the motion of boundaries. Obviously, the technique for moving the mesh is crucial in this method to achieve high robustness and high efficiency. For this purpose, a novel methodology is suggested and adopted, in which interior nodes and boundary nodes are considered separately; the nodes on the free surface and on rigid boundaries are considered separately; nodes on the free surface are split into two groups: those on waterlines and those not on waterlines (inner-free-surface nodes); and different methods are employed for moving different nodes.

To move the interior nodes which do not lie on boundaries, a spring analogy method is used. In this method, nodes are considered to be connected by springs and the whole mesh is then deformed like a spring system. Specifically, the nodal displacement is determined by

$$\Delta\vec{r}_i = \sum_{j=1}^{N_i} k_{ij}\Delta\vec{r}_j \Big/ \sum_{j=1}^{N_i} k_{ij}, \tag{23}$$

where $\Delta\vec{r}_i$ is the displacement at node I; k_{ij} is the spring stiffness and N_i is the number of nodes that are connected to node I. For problems about nonlinear water waves, it is crucial to maintain the quality (good element shapes and reasonable node distribution) of mesh near the free surface. To do so, the spring stiffness in the QALE-FEM is suggested as

$$k_{ij} = \frac{1}{l_{ij}^2} \mathrm{e}^{\gamma[1+(z_i+z_j)/2d]}, \tag{24}$$

where k_{ij} is the spring stiffness, l_{ij} is the distance between nodes I and J; z_i and z_j are the vertical coordinates of nodes I and J; d is the water depth; and γ is an coefficient that should be assigned a larger value if the springs are required to be stiffer at the free surface. The spring analogy method is also used for moving nodes on rigid boundaries.

The positions of nodes on the free surface are determined by physical boundary conditions, i.e., following the fluid particles at most time steps. The nodes moved in this way may become too close to or too far from each other. To prevent this from happening, these nodes are relocated at a certain frequency, e.g. every 40 time steps. When doing so, the nodes on the waterlines is re-distributed by adopting a principle for a self-adaptive mesh, i.e., the weighted arc-segment lengths satisfies

$$\varpi_i \Delta s_i = C_s, \tag{25}$$

where ϖ is a weighted function, Δs_i the arc-segment length between two successive nodes and C_s a constant. In order to relocate the inner-free-surface nodes, they are first moved using the spring analogy system in the projected plane of the free surface, resulting in new coordinates x and y; and then the elevations of the free surface corresponding to the new coordinates are evaluated by an interpolating method. In order to take into account of the local gradient of the free surface, however, the spring stiffness for moving the nodes in x- and y-directions is determined, respectively, by:

$$k_{ij}^{(x)} = \frac{1}{l_{ij}^2}\sqrt{1+\left(\frac{\partial\zeta}{\partial x}\right)^2} \quad \text{and} \quad k_{ij}^{(y)} = \frac{1}{l_{ij}^2}\sqrt{1+\left(\frac{\partial\zeta}{\partial y}\right)^2}, \tag{26}$$

where $k_{ij}^{(x)}$ and $k_{ij}^{(y)}$ are the spring stiffness; $\frac{\partial\zeta}{\partial x}$ and $\frac{\partial\zeta}{\partial y}$ the local slopes of the free surface in the x- and y-directions, respectively. The numerical tests in [1] have shown that the scheme for moving mesh is very robust and very efficient.

3.2. Calculation of fluid velocities on the free surface

The mesh used in the QALE-FEM is arbitrarily unstructured and moving during the calculation. An effective method to calculate the fluid velocity on the free surface under this condition is developed in [1]. In this method, the velocity at a node I with neighbours J_k ($k = 1,2,3,\ldots,m$) on the free surface is split into normal and tangential components. To estimate the normal component of the velocity, two points on the normal line at node I are selected firstly and the velocity potentials at these two points are then approximated by using a moving least square method. The normal component ($\vec{v}_n$) of the velocity is determined by a three-point finite difference scheme:

$$\vec{v}_n = \left[\frac{2}{3h_{I1}}\left(\frac{2h_{I1}+h_{I2}}{h_{I1}+h_{I2}}+\frac{1}{2}\right)\phi_I - \left(\frac{2}{3h_{I2}}+\frac{1}{h_{I1}}\right)\phi_{I1} + \frac{2}{3h_{I2}}\left(\frac{h_{I1}}{h_{I1}+h_{I2}}\right)\phi_{I2}\right]\vec{n}, \tag{27}$$

where $I1$ and $I2$ represent the two points selected; h_{I1} and h_{I2} are the distances between I and $I1$ and between $I1$ and $I2$, respectively; and ϕ_I, ϕ_{I1} and ϕ_{I2} denote the velocity potentials at the node and the two points; the later two, ϕ_{I1} and ϕ_{I2}, are found by a moving least square method. After the normal component of the velocity is determined, the tangential components of the velocity are calculated using a least square method based on the following equation:

$$\vec{v}_{\tau_x}\cdot\vec{l}_{IJ_k} + \vec{v}_{\tau_y}\cdot\vec{l}_{IJ_k} = \vec{l}_{IJ_k}\cdot\nabla\phi - \vec{v}_n\cdot\vec{l}_{IJ_k} \quad (k = 1,2,3,\ldots,m), \tag{28}$$

where $\vec{l}_{IJ_k}$ is the unit vector from node I to node J_k; $\vec{v}_{\tau_x}$ and $\vec{v}_{\tau_y}$ represent the velocity components in $\vec{\tau}_x$ and $\vec{\tau}_y$ directions, respectively. These directions are determined by $\vec{\tau}_x \perp \vec{n}$, $\vec{\tau}_x // \vec{e}_x$, $\vec{\tau}_y \perp \vec{n}$ and $\vec{\tau}_y // \vec{e}_y$, where $\vec{e}_x$ and $\vec{e}_y$ are the unit vectors in the x- and y-directions, respectively.

4. Mesh moving scheme associated with floating bodies

The new developments of this paper for dealing with problems with a 2D floating body will be presented in the next three sections. They mainly contain three aspects: (1) mesh moving when a floating body is involved; (2) calculation of fluid velocities on the surface of the floating body and (3) estimation of velocities of the floating body and forces on it. The first aspect is presented in this section.

The basic strategy and principle to move the mesh are similar to that for the problem without floating bodies as summarised above. Nevertheless, special considerations must be devoted to the mesh near the body and on its surface, which is discussed in the following two subsections.

4.1. Moving interior nodes

Interior nodes are moved by the spring analogy method, similar to that for problems without floating bodies as outlined above. However, with a floating body involved, the mesh must preserve a reasonable element shape and node distribution not only in the vicinity of the free surface but also in the region close to the

floating body, i.e. the near-body-region, as illustrated in Fig. 2. To achieve this, the springs near both the free and body surfaces are chosen to be stiffer than those in other areas, that is, Eq. (24) is replaced by

$$k_{ij} = \frac{1}{l_{ij}^2} e^{\gamma_f[1+(z_i+z_j)/2d]} e^{\gamma_b(\hat{w}_i+\hat{w}_j/2)}, \tag{29}$$

where γ_f is the same as γ in Eq. (24); γ_b plays the same role as γ_f but is used to adjust the spring stiffness near the body surface. The two coefficients may be different but in this paper they are taken to be the same values, i.e., $\gamma_f = \gamma_b = 1.7$. In Eq. (29), $\hat{w}$ is a weight function and is determined by,

$$\hat{w} = \begin{cases} 0, & d_f > D_f, \\ 1 - d_f/D_f, & d_f \leqslant D_f, \end{cases} \tag{30a}$$

where d_f is the minimum distance from the node concerned to the body surface as shown in Fig. 2; D_f is the distance between the body surface and the boundary of the near-body-region and is defined as,

$$D_f = \varepsilon d_{c\max}, \tag{30b}$$

where $d_{c\max}$ is the maximum distance from the gravitational centre to the wetted body surface and depends on the relative position of the floating body to the free surface. Numerical tests show that $\varepsilon = 1.5$ is suitable. It can be seen from Eqs. (29) and (30) that the spring stiffness outside the near-body-region is the same as that for problem without a floating body.

4.2. Moving nodes on body surfaces

The wetted body surface is time-dependent in the problems considered here. In order to conform to the change in the wetted body surface, the nodes on the surface must also be moved at each time step. The principle for doing so is similar to that for moving the nodes on the free surface, i.e., splitting the nodes into two groups: nodes on the waterline and nodes lying on the body surface but not on the waterline, the later called inner-body-surface nodes. For 2D problems, there are only two nodes on the waterline. They are moved by using the tangential velocity of the fluid relative to the body surface. The inner-body-surface nodes may appear to be moved by the same approach for moving inner-free-surface nodes, i.e., projecting the nodes onto a horizontal plane, moving the nodes in it by using the spring analogy method and then finding the new positions of nodes on the body surface by interpolation. This approach is obviously subjected to a condition that the surface must have only one intersecting point with any vertical line; in other words, it can be expressed by a single-valued function. However, this is not always true for floating body surfaces, particularly when they undergo angular motions, such as roll and/or pitch. Therefore, one cannot actually use the same approach as for moving the inner-body-surface nodes. A new approach is developed here. In this new approach, the spring analogy method is applied in a local coordinate system formed by the local tangential and normal lines. In this local coordinate system, the body surface is single-valued; i.e., there is only one intersecting point between the body surface and a line parallel to the local normal line (and, of course, perpendicular to the local tangential line). A node, e.g., i, is first moved along the tangential line by

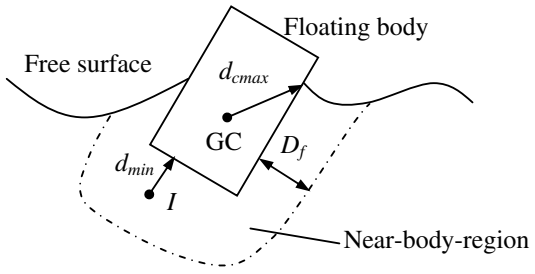

Fig. 2. Region near floating body (GC: gravitational centre).

$$\Delta\vec{r}_{i\tau} = \sum_{j=1}^{N_i} k_{ij}\Delta\vec{r}\cdot\vec{\tau}_i \Big/ \sum_{j=1}^{N_i} k_{ij}, \tag{31}$$

where $\vec{\tau}_i$ is the tangential direction at node i. After that, the new position of the nodes on the body surface is found by interpolation in the local coordinate system. The spring stiffness in Eq. (31) is taken as $k_{ij} = 1/l_{ij}^2$.

It should be noted that at a sharp corner, there will be no unique tangential and normal lines and so the above approach fails. The remedy for overcoming the difficulty is to prescribe a node at the corner or to smooth the corner. Either way works well and gives similar results based on our numerical tests. It should also be noted that the new approach described in this sub-section may be employed to move inner-free-surface nodes when overturning waves are involved, though they are not considered in the paper.

5. Calculations of fluid velocity on the surface of the floating body

The velocity potential on the floating body surface always satisfies Eq. (4) and so the normal components of fluid velocity on the body surface can be determined by

$$\vec{v}_n = \vec{n}\cdot\vec{U}(t) = \vec{n}\cdot(\vec{U}_c + \vec{\Omega}\times\vec{r}_b). \tag{32}$$

Eq. (28) is then used to estimate the tangential component of fluid velocity on the body surface. In 2D cases, it is similar to a central difference scheme at the inner-body-surface nodes. However, at the nodes on the waterline, it becomes similar to a backward scheme due to unsymmetrical distribution of nodes around the waterline and so becomes less accurate than at the inner-body-surface nodes. As an alternative, the tangential velocity at waterline nodes is estimated by using a three-point method similar to Eq. (27). The normal line required by Eq. (27) is taken as a line (τ_w) tangent to the body surface, as shown in Fig. 3. The three points contain the node on the waterline and other two points on the line τ_w. The velocity potentials at the two points (marked as empty circles in Fig. 3) are found using the same method as that for $I1$ and $I2$ in Eq. (27).

6. Calculation of forces on and velocities of the floating body

In this paper, $\partial\phi/\partial t$, involved in Eqs. (11) and (12) for estimating the forces on floating bodies, is calculated by solving a boundary value problem defined in Eqs. (15)–(17). As discussed in Section 2.3, there is difficulty with doing so due to the nonlinear coupling between the body and wave motions. In order to tackle this difficulty, four types of methods have been suggested in the literature, i.e. the indirect method, the mode-decomposition method, the Dalen and Tanizawa's method and the iterative method. The indirect method was developed by Wu and Eatock Taylor [16] and followed by Kashiwagi and Momoda [25] and Kashiwagi [26], Wu and Hu [27]. In this method, some auxiliary functions were introduced to decouple the mutual dependence between the force and the acceleration of the body. The mode-decomposition method was suggested by Vingi and Brevig [8] and adopted by Koo [23] and Koo and Kim [24]. In this approach, the body acceleration is decomposed into several modes (4 modes in 2D cases or 7 modes in 3D cases, respectively). Every mode is found by solving a boundary value problem similar to that for the velocity potential but under different boundary conditions. Using these modes and the body-motion equations, the body acceleration is determined. Both these methods have to solve 4 or 7 extra Laplace equations under different boundary conditions. The CPU time, therefore, may be considerably increased if employing an iterative procedure rather than a direct solution scheme (such as Gauss Elimination) which is unlikely to be suitable for solving the corresponding

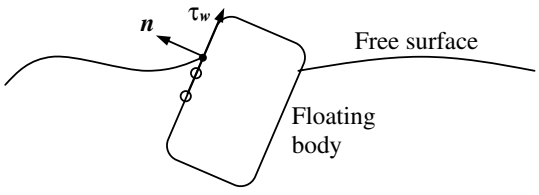

Fig. 3. Definition of tangential and normal directions at a node on the waterline.

linear algebraic system containing a very large number of unknowns. In the method proposed by Dalen [30] and Tanizawa in [20,31], the body accelerations in Eq. (17) are implicitly substituted by the Bernoulli's equations and thus the velocity potential and its time derivative are solved without the need of calculating accelerations of the floating bodies. However, this method requires one to form a special matrix for $\partial\phi/\partial t$ which is different from the one for the velocity potential and whose properties have not been sufficiently studied. This is likely to increase the difficulty for numerically solving the algebraic equations associated with $\partial\phi/\partial t$ and also needs more CPU time for generating the special matrix. That would be the main reason for this method not to be commonly used. Cao et al. [19] suggested an iterative method to calculate the force and acceleration at each time step; in this way, the need to solve extra equations in the first two methods and the problem with the third method is eliminated.

For the purpose of time marching, a standard explicit fourth-order Runge–Kutta scheme is generally used to update the velocity of the floating body, which requires three sub-step calculations at one time step forward. In each sub-step, the geometry of the computational domain may or may not be updated. If it is not updated, it is called a frozen coefficient method; if it is update, it is called a fully updated method. The CPU time spent on updating in the fully updated method is roughly equal to 4 times that in the frozen coefficient method. However, the frozen coefficient may not lead to stable and reasonable results for problems with large motions of floating bodies, as indicated by Koo and Kim [24].

The body velocity is estimated from the acceleration at previous time steps (or sub-steps) in all the above methods; i.e., the corresponding procedure is explicit. The explicit procedure may be satisfactory if time steps and so changes in the velocity and acceleration in one step are sufficiently small; otherwise, it may degrade the accuracy and even lead to instability.

In this paper, an improved iterative procedure, called iterative semi implicit time integration method for floating bodies (ISITIMFB), is developed, which takes some advantages and overcome some disadvantages of other methods. This method features by (a) using the acceleration in the current step to estimate the body velocity, i.e., it is implicit, distinguishing it from all other methods discussed above; (b) not requiring sub-step calculations, different from the fully updated Runge–Kutta method; (c) eliminating the necessity of solving the extra equations as in the indirect method and the mode-decomposition method and the need to generate a special matrix in the Dalen and Tanizawa's method, getting rid of the main disadvantages of all three; (d) not updating the positions of the free surface and the floating body during the iteration to find the acceleration and force, saving the CPU time spent not only on this but also on forming the new coefficient matrix. The details of the method are described as follows.

Suppose that all calculations until $t = t_{n-1}$ have been finished and so the velocity potential and its time derivative on the free surface, the positions of all boundaries including the free surface and the body surface have been obtained through updating. To find the fluid and body velocities at time t_n, the following procedure is used.

(1) Predict the body acceleration $\vec{A}^{n(0)}$ at time t_n by curve fitting of accelerations at previous time steps using a least square method [34] and estimate the corresponding body velocity by using the Adams–Moulton method [35] as following,

$$\vec{U}_b^{n(0)} = \vec{U}_b^{n-1} + \frac{\Delta t}{12}(5\vec{A}_b^{n(0)} + 8\vec{A}_b^{n-1} - \vec{A}_b^{n-2}), \tag{33}$$

where $\vec{A}^{n(0)}$ and $\vec{U}_b^{n(0)}$ represent the predicted values of translational or angular body accelerations and velocities, respectively, at the current time step, which are used as the initial values of iteration.

(2) Solve the boundary value problem for ϕ using $\vec{U}_b^{n(0)}$ in Eq. (4) for the boundary condition on the body surface.
(3) Calculate the fluid velocity and the time derivative of the velocity potential on the free surface.
(4) Calculate the fluid velocity $\vec{V}_b^{n(0)}$ on the body surface.
(5) Using the following loop to find the acceleration of and forces on the body:
   (a) Solve the boundary value problem for $(\frac{\partial\phi}{\partial t})^{n(k)}$ using $\vec{A}^{n(k-1)}$, $\vec{U}_b^{n(k-1)}$ and $\vec{V}_b^{n(k-1)}$ in its boundary condition on the body surface (Eq. (17)), where the subscript $n(k-1)$ represents the variables at time t_n but at kth iteration ($k = 1, 2, 3\ldots$).

(b) Calculate the forces or moments $\vec{F}^{n(k)}$ and so the acceleration

$$\vec{A}_b^{n(k)} = [M]^{-1}[\alpha^n \vec{F}^{n(k)} + (1-\alpha^n)\vec{F}^{n(k-1)}]; \tag{34}$$

in which mass matrix $[M]$ should be changed to the moment matrix of the mass $[I]$, (Eq. (8)), if the angular acceleration and moment are concerned.

(c) Estimate the new body velocity using the similar method to Eq. (33)

$$\vec{U}_b^{n(k)} = \vec{U}_b^{n-1} + \frac{\Delta t}{12}(5\vec{A}_b^{n(k)} + 8\vec{A}_b^{n-1} - \vec{A}_b^{n-2}). \tag{35}$$

(d) Solve the boundary value problem for ϕ using $\vec{U}_b^{n(k)}$ in Eq. (4) for the boundary condition on the body surface.

(e) Calculate the new fluid velocity $\vec{V}_b^{n(k)}$ on the body surface.

(f) Check if the relative error of accelerations (or forces) is small enough; if not, go to (a); otherwise go to (6).

(6) Update the position of the body using the final body velocity and acceleration in the above loop by using the third-order Taylor expansion,

$$\vec{S}_b^{n+1} = \vec{S}_b^n + \vec{U}^{n(u)}\Delta t + \frac{\Delta t^2}{2}\dot{\vec{U}}^{n(u)} + \frac{\Delta t^3}{6}\frac{\mathrm{d}\dot{\vec{U}}^{n(u)}}{\mathrm{d}t}, \tag{36}$$

where $\vec{S}_b^{n+1}$ is the translational or angular displacement of the body to be used for the calculation of the next time step; $\vec{U}^{n(u)}$ and $\dot{\vec{U}}^{n(u)}$ represent the final values of body velocities and accelerations (translational or angular) in the above loop, respectively; and $\frac{\mathrm{d}\dot{\vec{U}}^{n(u)}}{\mathrm{d}t}$ is calculated by using the finite difference scheme $\frac{\mathrm{d}\dot{\vec{U}}^{n(u)}}{\mathrm{d}t} = (\dot{\vec{U}}^{n(u)} - \dot{\vec{U}}^{n-1(u)})/\Delta t$.

(7) Calculate the fluid velocity on the free surface using the final velocity potential in the above loop.

(8) Update the time derivative of the velocity potential on and the positions of the free surface using the same method as in [5,18].

(9) Go to next time step.

As can be seen, an under-relaxation in Eq. (34) is employed in the iterative loop from (a) to (f) to improve the convergent efficiency. The value of α^n is determined by

$$\alpha^n = \frac{A_b^{n-1(u)} - A_b^{n-1(0)}}{A_b^{n-1(1)} - A_b^{n-1(0)}}, \tag{37}$$

where $A_b^{n-1(u)}$ is the final value of the acceleration in the iteration at the previous step. This expression is proposed by considering the fact that if one had known α^{n-1}, the solution for $A_b^{n-1(u)}$ would have been found in one iteration through (a)–(f) and by assuming that $\alpha^n \approx \alpha^{n-1}$.

The efficiency of the iterative procedure is signified by the iteration counter (or the number of iterations) in the above loop – the smaller iteration counter the more efficient. One may understand that the iteration counter for a specified accuracy depends on the quality of the predicted velocity in Eq. (33) and three values of the acceleration in Eq. (35). The better prediction of the velocity and the closer values of the acceleration should lead to the smaller number of iterations. The quality of the predicted velocity and the values of the acceleration are in turn determined by the time step, the amplitude of the body motions and the natural frequency of the system. It is expected that the velocity is better predicted and three values of the acceleration becomes closer and hence the iterations is fewer if the time step and the amplitude are smaller and/or if the natural period is larger. For the given wave and the shape of the body, the largest motion amplitude is related to the natural period. Therefore, the two most important factors affecting the iteration counter may be the time step and the natural period. Their effects are to be investigated in Section 7.2.2.

This iterative procedure is distinguished from one in [19] by three aspects: (1) The velocity potential (and so the fluid velocity) is obtained in [19] by assuming that the body velocity in Eq. (4) is estimated using the acceleration at the previous time step and thus the boundary value problem for ϕ is solved only once, i.e. without step (d), in the above loop. Therefore, the procedure in [19] is actually an explicit method as implied above. (2)

The relaxation scheme in Eq. (34) and the corresponding relaxation coefficient in Eq. (37) are employed in this paper while it is not clear whether any relaxation is adopted in [19]. (3) The body velocity used in Eq. (4) is continually updated here by employing the scheme as given in Eqs. (33) and (35), while it needs to be evaluated only once in [19].

It has been pointed out that the body and free surface positions are not updated in the iteration loop in the above procedure. That is why this method is classified as 'Semi Implicit'. In this aspect, it is similar to the frozen coefficient method. However, this procedure has not been found to suffer the instability problem associated with the frozen coefficient method; instead, it has been found to share the similar stable behaviour with the full updated Runge–Kutta method. Numerical demonstration of this will be given below.

7. Validations and discussions

In this section, the QALE-FEM method is validated by comparing its numerical predictions with analytical solutions and published results from other papers. Unless mentioned otherwise, the parameters with a length scale are nondimensionalised by the water depth d; and other parameters, including the time and frequency, by

$$t \to \tau\sqrt{d/g} \quad \text{and} \quad \omega \to \omega\sqrt{g/d}.$$

7.1. Forced-motion bodies

Although the main aim of this paper is to simulate cases involving 2D free-response floating bodies, the case for a 2D body in forced motions is investigated in the first stage in order to validate the force calculation, in which the iteration loop discussed in the previous section becomes unnecessary since the body acceleration does not need to be found. The body in these cases is formed with a circular cylinder as the submerged part and vertical walls above it, as shown in Fig. 4a. The dimensionless radius of the cylinder ($\overline{R}_b$) is 0.25. The initial mesh around the body is similar to that in Fig. 4b but much finer.

The displacement (η) of the body is specified by

$$\eta(\tau) = a_b \sin(\omega_b \tau), \tag{38}$$

where a_b and ω_b are the amplitude and circular frequency of the motion, respectively. The velocity corresponding to Eq. (38) is $\vec{U}_c(\tau) = a_b\omega_b \cos(\omega_b\tau)$. This implies that the floating body suddenly gain a finite value of velocity from rest, which is not only practically impossible but also can result in a numerical difficult [32,33]. To avoid it, the velocity $\vec{U}_c$ is ramped as in [33] and given by

$$\vec{U}_c(\tau) = a_b\omega_b \cos(\omega_b\tau)(1 - e^{\beta\tau}), \tag{39a}$$

$$\beta = -\chi\omega_b/2\pi, \tag{39b}$$

where χ is a coefficient. The larger the value of χ, the shorter the time is, during which the effects of the ramp function persist, though the value does not affect the final results. In this paper, $\chi = 5$ is used.

7.1.1. Comparison with the analytical solution

When the amplitude of the harmonic motion is small, the hydrodynamic force can be evaluated by summing the analytical added mass and radiation damping forces [36], which is used for comparison with numerical

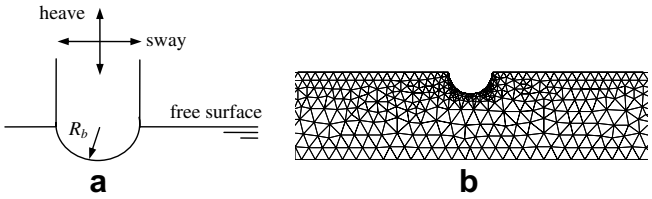

Fig. 4. Sketch of body motions and illustration of initial mesh: (a) floating body, (b) initial mesh near the body.

results to verify our method. For the numerical simulation, the total tank length is taken as $L \approx 30$ with the length from the wavemaker to the body taken as $L_w \approx 15$ (Fig. 1). The motion amplitude in Eq. (38) is assigned as $a_b = 0.01$. The mesh is unstructured and there are about 35 elements on the free surface in each wave length. The time step is taken as $T/128$, where T is the wave period. The x-direction hydrodynamic force (divided by $\rho g d^2$) in the forced sway and the z-direction hydrodynamic force (also divided by $\rho g d^2$) in the forced heave are plotted in Fig. 5 for three cases with different values of ξ, where $\xi = \omega_b^2 \overline{R}_b$ is the frequency parameter. It can be seen that the numerical results agree very well with the analytical ones in all the cases, except in the transient period when the difference is expected because the analytical forces are evaluated for steady state but not for the transient stage. To quantitatively show the accuracy of the numerical results, the relative error (E_r) for the results in Fig. 5 is evaluated by:

$$E_r = \frac{\|f_n - f_a\|}{\|f_a\|}, \tag{40}$$

where $\|f\| = \int_{A_e} f^2 \, dA$; f_n and f_a are the numerical and analytical forces, respectively; and A_e is the duration over which the error is estimated. Because the accuracy of the forces within the transient period should not be of concern, A_e is taken as the total duration of simulation minus the transient period (about half of wave period). The relative errors evaluated in this way for all the cases in Fig. 5 do not exceed 0.5%.

The characteristics of the relative error are further investigated by considering different time steps and different mesh sizes. For this purpose, the relevant parameters are taken as $a_b = 0.01$ and $\xi = 0.75$ (the corresponding wave length is about $\lambda \approx 2.0$), which are the same as the second case in Fig. 5. It should be noted that the investigation on how numerical errors are affected by time steps is relatively easy but not on how they are related to mesh sizes. That is because the errors depend on both mesh sizes and mesh structures and also because it is impractical to consider all possible mesh structures as the unstructured meshes are used in this paper. Apart from these, the mesh sizes constantly change with time for water wave problems. To eliminate the difficulty, a representative mesh size (ds) is used, which is defined as the distance between nodes on the free surface when the water is at rest. The initial mesh structures are almost the same in all cases considered, which feature that the nodes on the free surface, the tank bed and the body surface are uniformly distributed; the distance between nodes on the free surface is roughly twice of that on the body surface and half of that on

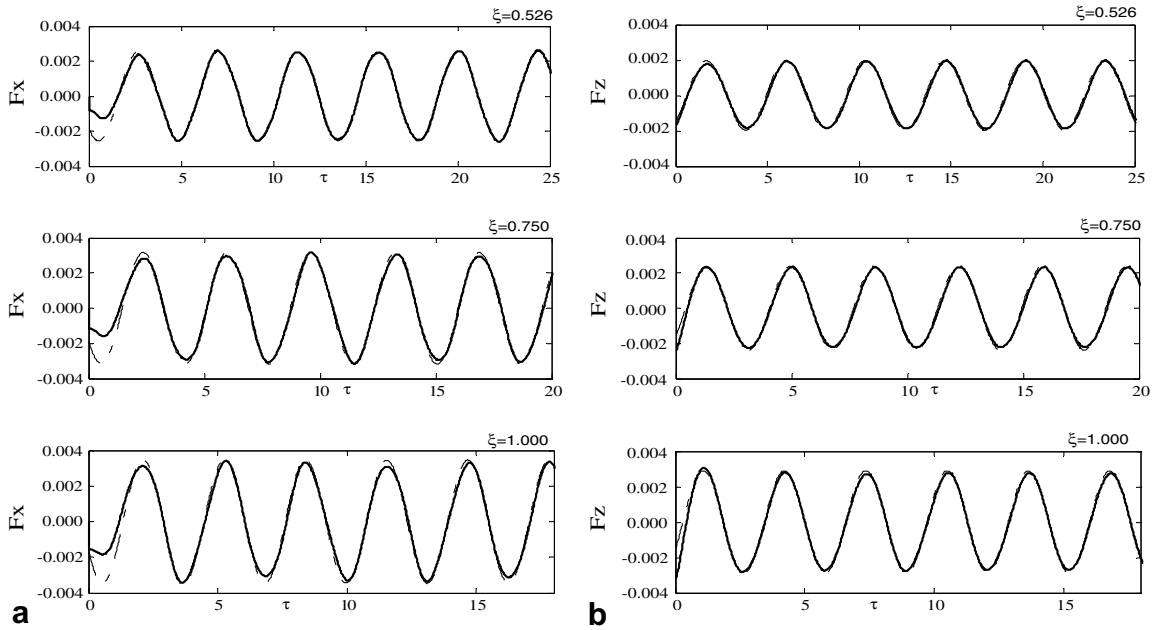

Fig. 5. Comparison of force histories for cases for forced sway/heave with analytical solution (solid line: numerical results, dot line: analytical solution [36]): (a) forced sway, (b) forced heave.

the tank bed; and the distance between nodes in the vertical direction gradually decrease from the bed to the free surface. The relative errors corresponding to different time steps and different representative sizes (ds) are presented in Figs. 6a and b for sway and heave, respectively. In these figures, the time step is given as the wave period (T) divided by a number. It is observed that the relative errors are reduced with the decrease in mesh sizes and/or time steps, as expected. Particularly in the ranges of $0 < ds < 0.057$ (about 35 elements in over one wave length) and $0 < dt < T/64$, the relative errors are less than 0.8% for all these cases. This implies that the numerical results with a specified accuracy are achievable by using a sufficiently fine mesh and small time step.

7.1.2. Forced motion with larger amplitudes

In order to investigate the nonlinear effects on waves generated by the forced-motions of the floating body, the cases similar to Fig. 5 but with larger amplitudes are simulated. The wave histories recorded on the left-hand side of the body for the case with forced sway ($a_b = 0.123$) are depicted in Fig. 7 together with that for $a_b = 0.0041$. Fig. 8 shows the wave histories for the forced heave, in which the solid line is the wave history for $a_b = 0.082$, while the dot line is that for $a_b = 0.0041$. In both figures, the wave elevations are divided by the motion amplitude (a_b).

It can be observed that the wave height seems not to be changed dramatically while the shape of the wave history curve becomes more complicated as the amplitudes of motions becomes larger in the cases for forced sway. In the cases for forced heave, the wave history becomes sharper at crests and flatter at troughs with the increase of the motion amplitudes. All are typical features of nonlinear waves. To show how well the mesh conform to the variation of the body and free surfaces, the mesh configurations for forced sway motions at some time steps are given in Fig. 9. From these figures, it can be seen that the mesh quality near the body surface is maintained even though the motion of the floating body is large. This implies that the suggested method to move nodes works well in the cases including the floating bodies and the free surface.

7.2. Free-response floating bodies

After being validated by using cases for forced-motions, the QALE-FEM method is now applied to simulate the motions of a 2D free-response floating body. The incident waves are generated by a wavemaker in a tank and the body is moored to the walls of the tank, as illustrated in Fig. 1. The initial mesh used is similar to Fig. 4b but the circular cylinder is changed to a barge-type floating body. For this body, the mass is 125 kg; the moment of inertia about the gravitational centre is 4.05 kg m^2; the width (B_b) is 0.5 m; the draft is 0.25 m; the local radius of round corner of the body is 0.064 m and the gravitational centre is located at 0.885 m measured from the keel of the barge. In this paper, the mooring line is modelled by a horizontal spring through the gravitational centre with the spring stiffness taken as 197.58 N/m. These parameters and the shape of the body are

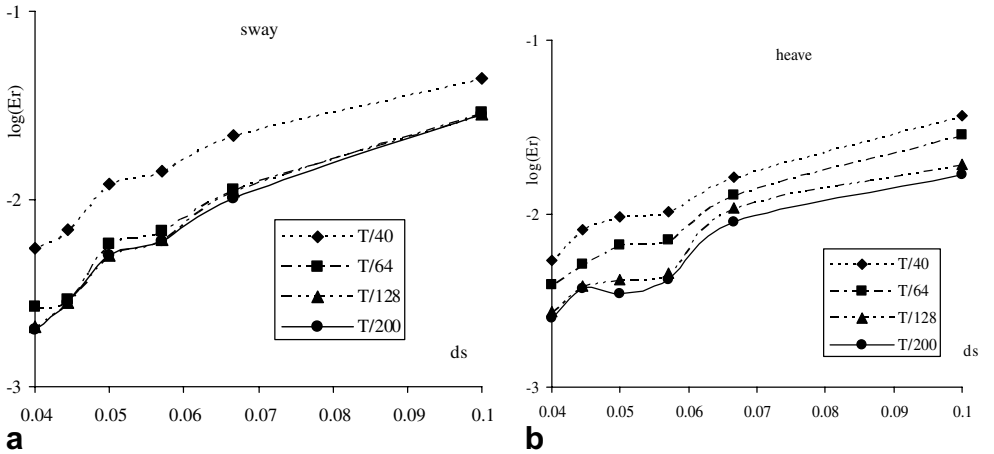

Fig. 6. The relative error for different meshes and different time steps: (a) sway, (b) heave.

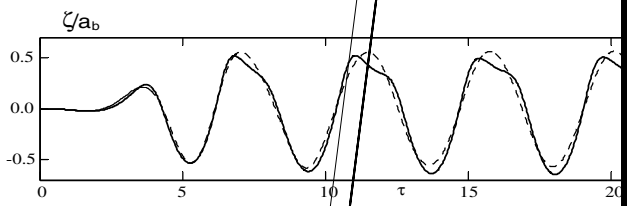

Fig. 7. Wave history recorded at $x = -1$ due to forced sway ($L = 30$, $\omega_b = 1.45$, $\xi =$

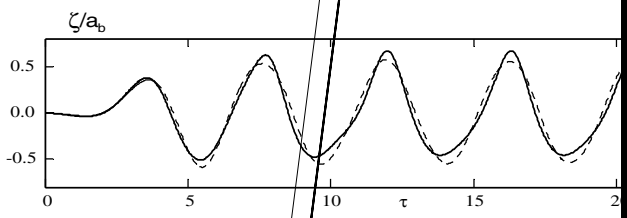

Fig. 8. Wave history recorded at $x = -1$ due to forced heave ($L = 30$, $\omega_b = 1.45$, $\xi =$

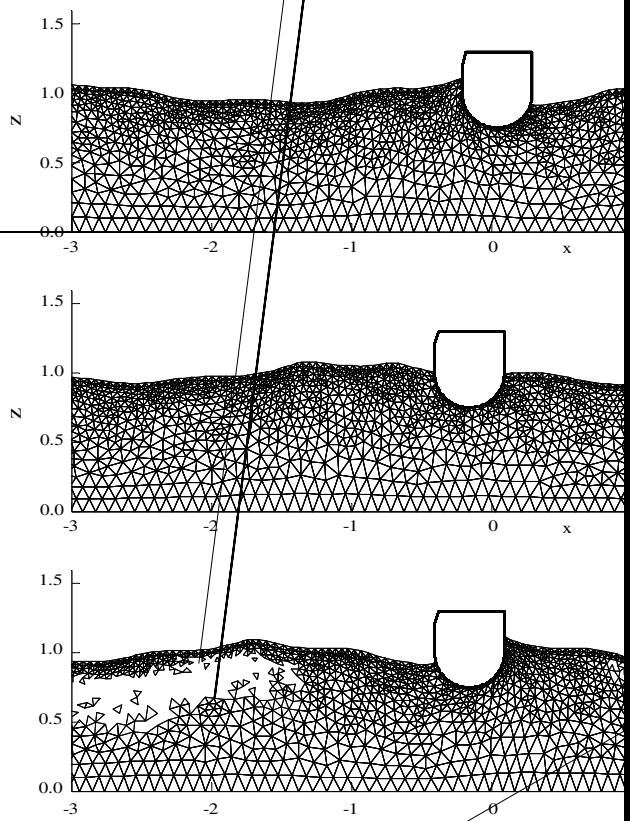

chosen to be consistent with those in [24,37], whose results will be us
tion 7.2.3. In the simulations, the average water depth of the tank is
$\lambda = \frac{2\pi g}{\omega^2}\tanh(2\pi)$. In the following presentation, the frequency (ω) of
$\xi = \omega^2 B_b/2g$; the force is nondimensionalised by using $\rho g d^2$ on the as
in the direction parallel to the wavemaker is unit; and the roll angle is

A_w is the amplitudes of incident waves. Other parameters are nondimensionalised by the same way as in previous sections.

7.2.1. Wavemaker ramp function and artificial damping technique

It is well known that the waves generated by a wavemaker in a tank are characterised by a transient wave profile in the front part of a wave train even though the motion of the wavemaker is purely harmonic. The transient wave profile often consists of several waves with different lengths and heights and a larger wave crest separating the transient and steady parts in the wave train. If one aims to investigate the properties of steady-sate responses, such as RAOs, of floating bodies, the transient waves and corresponding body responses are useless and hence they should be suppressed in order to reduce computational cost. Three methods may be used for this purpose. The first one is to apply wavemaker ramp functions that reduce the wave heights in the transient part. The second is to add artificial viscosity in the dynamic equations of floating bodies (called artificial damping technique), which diminishes the transient body responses. The third method is the combination of the first and the second ones. Details about them are given below.

Two wavemaker ramp functions are investigated, which are similar to those in [32,33]. The wavemaker motion corresponding to the first ramp function, called 'Ramp1', is governed by

$$S_w(\tau) = -a\cos(\omega\tau), \tag{41a}$$

$$U_w(\tau) = a\omega\sin(\omega\tau), \tag{41b}$$

$$\dot{U}_w(\tau) = a\omega^2\cos(\omega\tau)(1 - e^{\beta\tau}), \tag{41c}$$

where S_w, U_w and $\dot{U}_w$ are the displacement, velocity and acceleration of the wavemaker, respectively; and the coefficient β is the same as that in Eq. (39) with ω_b replaced by ω. In this approach, the generated wave is not modified by the ramp function because the velocity of the wavemaker and so the velocity potential are not affected. The ramping is only performed on the acceleration of the wavemaker, which implies that the value of $\partial\phi/\partial t$ and so forces on bodies are ramped. The wavemaker motion corresponding to the second ramp function, called 'Ramp2', is governed by

$$S_w(\tau) = -a\cos(\omega\tau)r(\tau), \tag{42a}$$

$$U_w(\tau) = \partial S_w/\partial\tau, \tag{42b}$$

$$\dot{U}_w(\tau) = \partial U_w/\partial\tau, \tag{42c}$$

$$r(\tau) = \begin{cases} 1, & \tau > T_f, \\ [1 - \cos(\pi\tau/T_f)]/2, & \tau \leqslant T_f, \end{cases} \tag{43}$$

where T_f is the cut-off time of the ramp function and is determined by

$$T_f = \kappa L_w/C_g \tag{44}$$

in which κ is a coefficient between 0 and 1; and C_g is the group velocity of waves.

The efficiency of Ramp1 and Ramp 2 is investigated with $\xi = 1$, $a = 0.0016$, $L \approx 15$ and $L_w \approx 10$. The mesh used is unstructured with about 35 elements on the free surface in each wavelength. For the Ramp2, $\kappa = 0.25$ and $\kappa = 0.5$ are adopted for two cases, respectively.

Fig. 10 shows the sway motions obtained by using different ramp functions. It can be observed that Ramp2 can make the calculation become steady sooner than Ramp1, though its effectiveness depends on the value of κ. It should be noted, however, that the waves at the wavemaker generated by using Ramp2 during period $\tau < T_f$ are not the incident waves desired, implying that the waves at the floating body do not become the desired incident waves until $\tau > T_f + L_w/C_g$. In addition, even after the desired incident waves arrive at the floating body, its responses exited by undesired waves do not disappear immediately and so take extra time (T_e) to become those excited by the desired waves. As a result, the time history of motions during the time $\tau < T_f + L_w/C_g + T_e$ should not be considered when estimating RAOs. Based on this analysis, it is obvious that the shorter the sum of $T_f + T_e$, the less CPU time is required for estimating RAOs. As can be seen in Fig. 10, the transient period becomes longer, indicating that T_e becomes larger, with T_f being shorter (i.e., smaller κ) when using the Ramp2 only. Therefore, the reduction in T_f does not necessarily lead to the reduction in the sum of $T_f + T_e$. The other

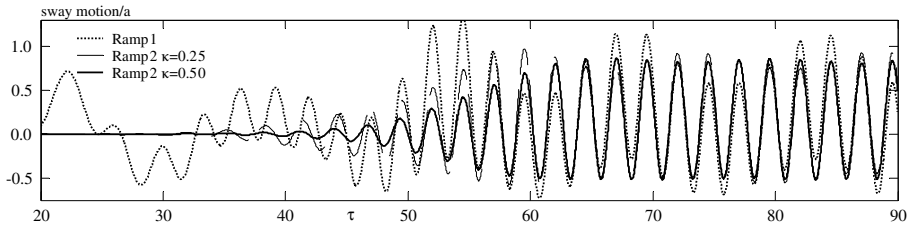

Fig. 10. Sway motion by using different ramp functions.

option left to us is to reduce T_e by using the artificial damping technique mentioned above. With this technique, the motion equation, e.g., Eq. (5a), is modified to

$$[M]\dot{U}_c + \beta_a U_c = F, \tag{45}$$

where β_a is the artificial damping coefficient. It is given by

$$\beta_a(\tau) = \begin{cases} 0, & \tau > T_d, \\ \alpha\beta_c[1+\cos(\pi\tau/T_d)]/2, & \tau \leqslant T_d, \end{cases} \tag{46}$$

where β_c is the critical damping corresponding to a motion component (such as sway or heave); α is a coefficient; and T_d is the time during which the artificial damping is active. It is found by numerical tests that $T_d = L_w/C_g$ and $\alpha = 0.5$ are appropriate for applications in this paper. Although this technique may be used alone, we will only discuss numerical results obtained by combining it with the Ramp2 to shorten the length of the paper.

To show the effectiveness of the combined method, the two cases for the Ramp2 with $\kappa = 0.25$ and $\kappa = 0.5$ in Fig. 10 are considered again but in the first case, both the Ramp2 with $\kappa = 0.25$ and the artificial damping technique with $\alpha = 0.5$ are applied. Fig. 11 gives the results, in which the dashed line denotes the result from the combined method while the solid line represents the result obtained by only using the Ramp2 with $\kappa = 0.5$. It is interesting to see that the response by the combined method using $\kappa = 0.25$ becomes steady at about $\tau = 60$, approximately two wave periods earlier than that by the Ramp2 alone with $\kappa = 0.5$, which is steady at about $\tau = 65$. However, as shown in Fig. 10, the response corresponding to $\kappa = 0.25$ becomes steady much later than that to $\kappa = 0.5$ when using the Ramp2 alone. This indicates that the combined method is more effective to suppress the transient response.

Apart from these given above, the hydrodynamic forces acting on the body obtained by using different ramp functions and/or the artificial damping technique are also investigated. The results are plotted in Fig. 12. It shows that no matter which method is used, the hydrodynamic force acting on floating body tends to the same steady-state limit. This result indirectly indicates that the wavemaker ramp function and artificial damping technique do not affect the RAOs.

7.2.2. The convergence properties of the ISITIMFB

One of developments in this paper is the suggestion of the ISITIMFB procedure to find the forces and the motions of the floating body. Its convergence properties, i.e. the iteration counter to achieve a specified accuracy, are presented and discussed in this subsection for the following case: the barge is similar to the one described at the beginning of Section 7.2; the length of the numerical tank is taken as $L \approx 13$ with $L_w \approx 8$;

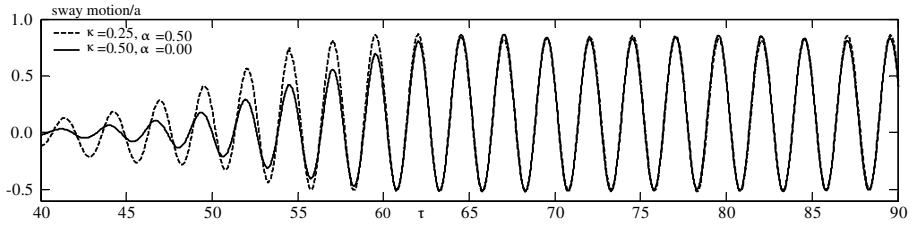

Fig. 11. Sway motion by using artificial damping technique.

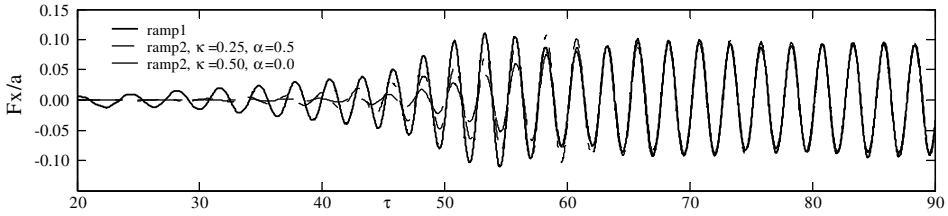

Fig. 12. Hydrodynamic force in cases with different ramp functions.

and the dimensionless incident wave height generated is about 0.018 and the frequency parameter is $\xi = 0.4$. Similar to above cases, the mesh used is unstructured with about 35 elements on the free surface in each wavelength. As has been discussed in Section 6, the two most important factors affecting the iteration counter are the time step and the natural period (frequency) of the system. Thus we mainly look at the convergence properties by changing the time step and the natural period in the following.

The results for different time steps are presented by three curves in Fig. 13a, which correspond to three specified relative errors: 0.1%, 0.5% and 1%. In the figure, there are two rows of numbers under the horizontal axis. The first row represents the number of time steps in each wave period and the second row gives the length of the time step, i.e. the period divided by the number in the first row. In these cases, the mass of the floating body is the same as before, i.e. 125 kg. Under this condition, the value of ξ based on the natural frequency is about 0.5–0.6 as shown by the experimental data in [24]. One may observe from this figure that the iteration counter for a specified error decreases with the increase in the number of time steps in each period as expected. One may also observe that the convergence can be achieved within 10 iterations when the control error is 1% and the number of time steps in each period is larger than 64; and that reducing the control errors leads to the increase of iteration but not significantly. It should be noted that the wave frequency is near the natural frequency in these cases. For other cases (not presented) where the wave frequencies are much larger than the natural frequency, the convergence properties are better than those shown here.

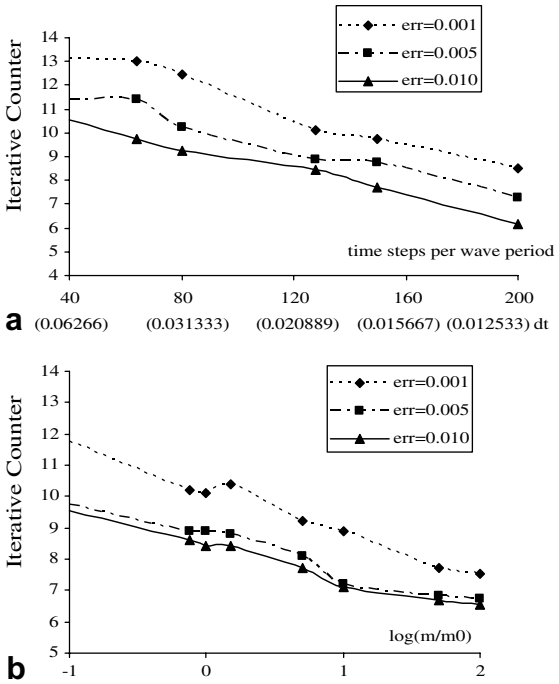

Fig. 13. Iteration counters for different time steps and different masses (err: the control iterative error): (a) iteration counter vs. time step, (b) iteration counter vs. mass.

The results corresponding to the different natural frequencies at three different control errors are depicted in Fig. 13b, which are obtained by artificially changing the mass in the range of $0.1m_0 \leqslant m \leqslant 100m_0$ (m_0: the mass for Fig. 13a) without changing the mooring stiffness and the shapes of the floating body (i.e., the restoring coefficient being roughly fixed). Under this condition, the square of the natural frequency should be inversely proportional to the mass; and on this basis, the iteration counter is plotted against the ratio of the mass to m_0 rather than the frequency in the figure. The time step is taken as $T/128$ and all other parameters are the same as those in Fig. 13a. The results in Fig. 13b indicate that the iteration counter varies with the change in mass or natural frequency but only in a small range for a large range of change in mass. Similar to Fig. 13a, the difference in the iteration counter does not change dramatically when the control error change from 0.1% to 1%. In addition, the iteration counter is smaller than 10 in the whole range of mass investigated for the control error of 1%.

Another point that needs to be discussed is how the control error in the ISITIMFB procedure affects the computed responses. Fig. 14 shows the comparison of roll motions obtained by using two different control errors for the cases of $\Delta t = T/64$ in Fig. 13. It can be seen that the difference between the results is negligible. Therefore, one may consider the control error of 1% is acceptable in engineering practice but it is recommended that the computed results are compared with those by using a smaller control error such as 0.5%, which is followed when acquiring the numerical results in the paper.

7.2.3. Comparison with other force calculation methods

In this subsection, the ISITIMFB procedure is firstly compared with a fully explicit method obtained by replacing Eq. (35) with an explicit Adams–Bashforth scheme [35],

$$\vec{U}_b^{n(k)} = \vec{U}_b^{n-1} + \frac{\Delta t}{2}(3\vec{A}_b^{n-1} - \vec{A}_b^{n-2}).$$

For the fully explicit method, the iteration is not needed. The time step is taken as $T/200$ and $T/64$; and other parameters are the same as those used in Fig. 14. The results are plotted in Fig. 15. From Fig. 15a, it is

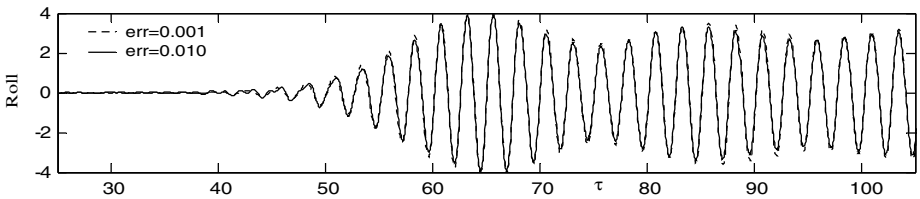

Fig. 14. Comparison of roll histories for different control errors ($dt = T/64$).

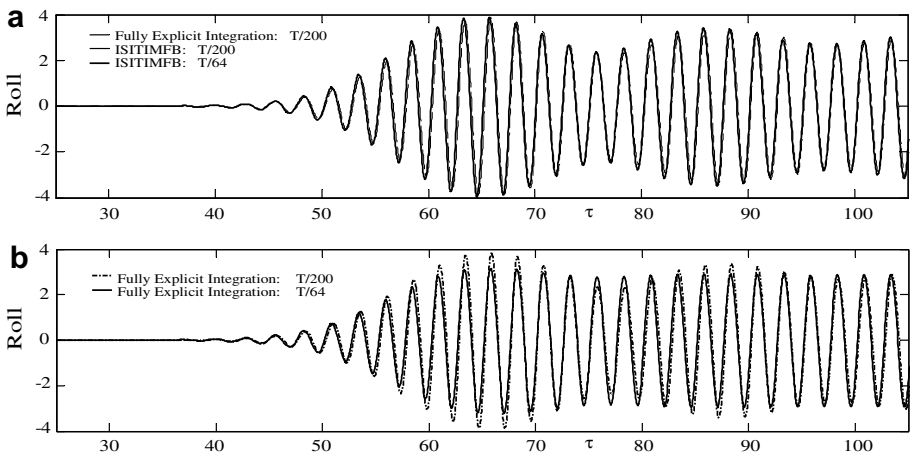

Fig. 15. Comparison of roll motions from the ISITIMFB and explicit procedures.

observed that the ISITIMFB leads to similar results to the fully explicit integration procedure when the time step is small ($T/200$). However, when the time step becomes larger ($T/64$), the results from the ISITIMFB have negligible difference from those for smaller time steps while the results from the fully explicit integration procedure poses evident disagreement with those using smaller time step (Fig. 15b). This indicates that the ISITIMFB proposed in this paper can give more accurate results at the same time step or can use larger time steps for specified accuracy and so needs less CPU time for a given period of simulation than the explicit method.

To further demonstrate the behaviours of the ISITIMFB, its results are then compared with those from fully-updated and frozen-coefficient fourth-order Runge–Kutta schemes [23] and shown Fig. 16, using the same parameters except for the wave height and the time step as for Fig. 15. To consider the same case as in [23], the dimensionless incident wave height of 0.0025 and the time step $\Delta t = T/40$ are used here. As can be seen, the presented procedure leads to steady-state results that agree well with those from the full-updated Runge–Kutta method while the frozen-coefficient Runge–Kutta scheme does not give similar results even when the time step is as small as $T/128$. The results for the frozen-coefficient Runge–Kutta scheme also tends to be unstable as indicated in [23]. This clearly demonstrates that the ISITIMFB can alleviate the instability problem of the frozen-coefficient method and can be as accurate and robust as the full-updated Runge–Kutta method but without the need of multiple updating of fluid domain geometries and so of the coefficient matrix in one time step forward.

7.2.4. RAOs of sway, heave and roll motions

To further validate the QALE-FEM method in the cases with a floating body, the RAOs of sway, heave and roll motions of the barge are compared with the linear solution by using frequency domain analysis as given in [24] and the experimental data in [37]. In the numerical simulations, Ramp2 together with the artificial damping technique is employed, for which the associated parameters are taken as $\kappa = 0.25$, $T_d = L_w/C_g$ and $\alpha = 0.5$; as in above sections, the unstructured mesh is adopted with about 30 elements on the free surface in each wavelength and the time step is taken as $\Delta t = T/128$. For all cases considered here, the amplitudes of the wavemaker are adjusted properly so that generated incident wave heights are either 0.01 or 0.07 m, which are the same as those in the cited publications.

The RAOs of sway, heave and roll motions corresponding to different incident waves are plotted in Fig. 17 together with the results from other publications. They are estimated by performing the FFT analysis on the steady-state portion of the time histories of corresponding motions. As can been seen, the present numerical results are closer to the linear solution when the incident waves are small (0.01 m) but closer to the experimental data when the wave height becomes larger (0.07 m). This is reasonable because the experimental data for the larger wave height contain nonlinear effects that are taken into account by the nonlinear numerical simulations but not by the linear solution.

However, the difference between experimental data and numerical results is obvious in the area near resonance frequencies. That may be due to the fact that the viscosity is not considered in numerical simulations whereas it is inevitable in experiments. To demonstrate that the conjecture might be true, an empirical damping force is added into the roll equation, which is formed by a damping coefficient multiplying the roll velocity. The value of the damping coefficient is taken as 1.5% or 2.8% of the critical damping coefficient in two different simulations. It should be noted that the empirical damping added here plays different rules and is for different purposes from the artificial damping discussed above. The empirical damping here is applied from the

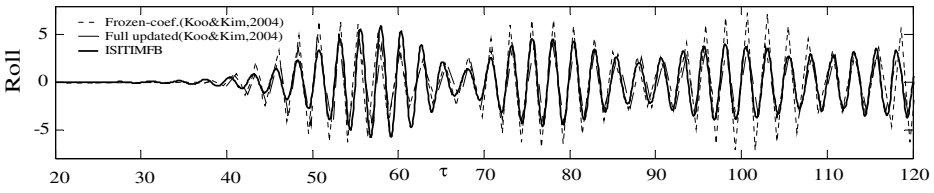

Fig. 16. Comparison of roll motions from ISITIMFB and other methods (frozen-coefficient scheme: $\Delta t = T/128$; ISITIMFB and fully updated Runge–Kutta method: $\Delta t = T/40$).

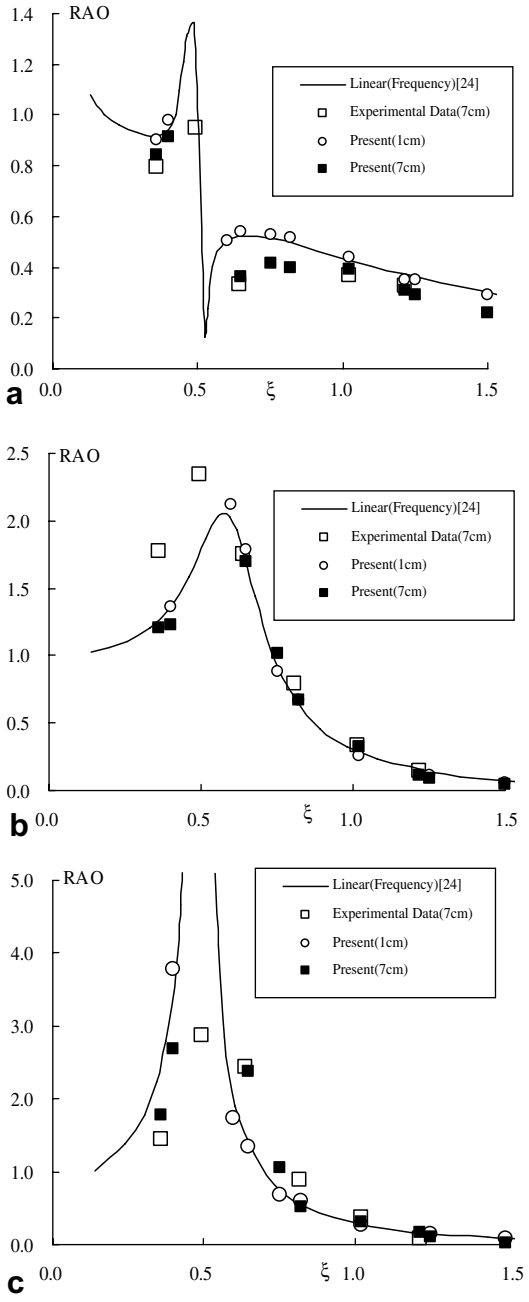

Fig. 17. RAOs of sway, heave and roll as a function of ξ: (a) RAO of sway motion, (b) RAO of heave motion, (c) RAO of roll motion.

start to the end of simulations to approximately model the real viscosity and so affects the amplitudes and RAOs even after the motions become steady. The artificial damping discussed in Section 7.2.1 is applied in a specified simulation period from the start in order to suppress the transient responses and does not affect the amplitudes and RAOs after motions become steady.

The RAOs of the roll motion near the resonant frequency obtained by using different empirical damping for the same cases in Fig. 17 are shown in Fig. 18 together also with the linear solution and the experiment data. It can be seen that when the empirical roll damping is 2.8% of the critical damping, our numerical results agree quite well with the experimental data in the resonant area in this case. Based on this, one may envisage that

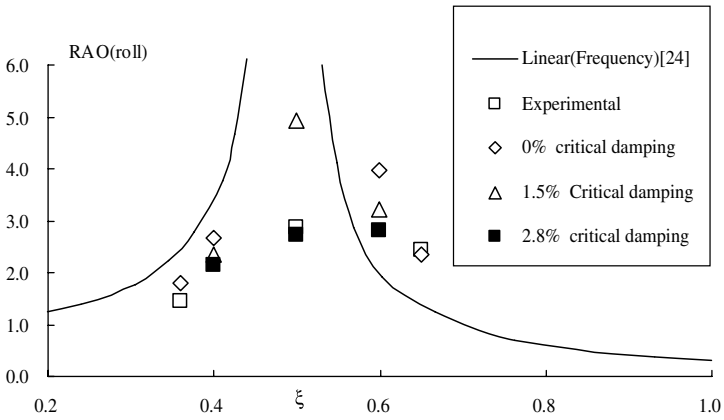

Fig. 18. RAO of roll motion in case with roll artificial damping.

with an appropriate empirical roll damping, our numerical method can give good approximate results even when the viscosity plays an important rule.

The cases in Figs. 17 and 18 are also simulated by using different meshes, different iterative control errors and different time steps. Some results are shown in Fig. 19, from which one can see that the difference between them is invisible. This signifies that the numerical errors due to selecting different mesh sizes, time steps and iterative control errors are negligible for the results in these two figures.

7.2.5. Transient responses of floating bodies

So far, discussions about responses of floating bodies to waves have been focused on the RAOs and how to calculate them in a more efficient way. In this section, some results are presented for transient responses of

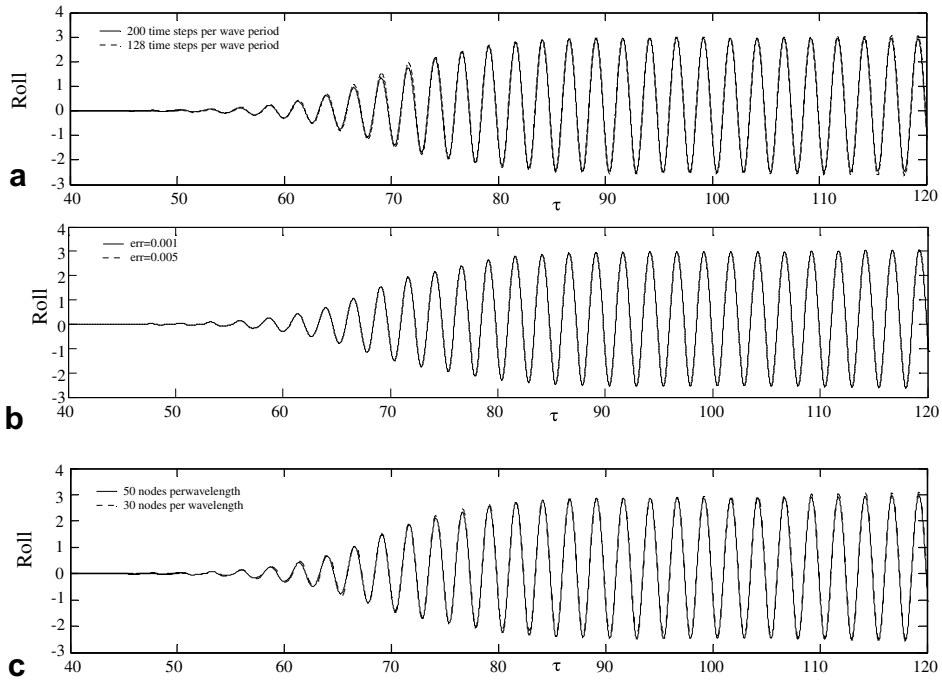

Fig. 19. Roll motion in terms of different time steps, iterative control error and meshes ($\xi = 0.5$, the wave height is 0.07 m): (a) different time steps (iterative control error is taken as 0.005, 30 nodes per wave length), (b) different iterative control errors ($\Delta t = T/128$, 30 nodes per wave length), (c) different meshes ($\Delta t = T/128$, iterative control error is taken as 0.005).

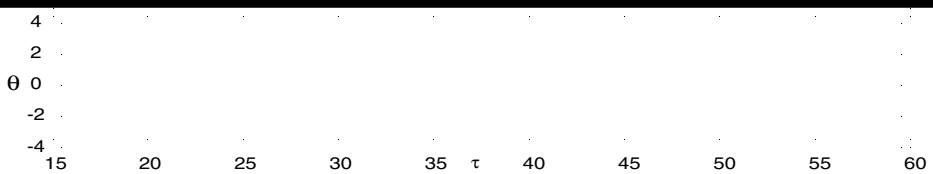

Fig. 21. Time history of roll for the wave height of 7 cm and $\xi = 0.65$.

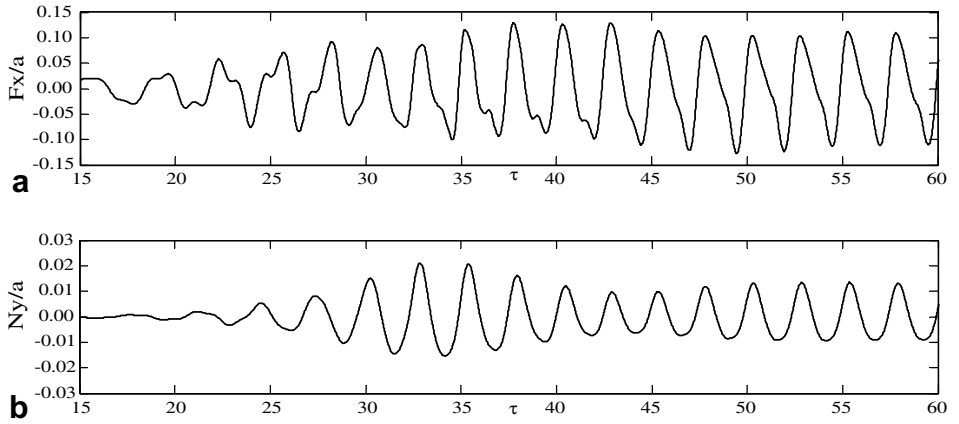

Fig. 22. Force and moment acting on the floating body ($\xi = 6.5$, the wave height is about 7 cm): (a) sway force, (b) roll moment.

To show the nonlinear effects in this case, the sway force and roll moment acting on the floating body is plotted Fig. 22. It can be observed that all the curves are quite complex. For the sway force, the curve in one wave period is not symmetric about the apex point in that period. For the roll moment, the curve exhibits the sharper high crests and flatter and shallower troughs. All are features of nonlinearity.

8. Computational efficiency of QALE-FEM for cases with free-response floating bodies

The significant development of the QALE-FEM is that the unstructured mesh is moved to conform to the motion of boundaries. As indicated in [1], without floating bodies, the mesh quality can be kept well. With the inclusion of floating bodes, their motions, particularly large angular motions, can make the mesh near body surfaces undergo large variations and so it is necessary to check if the methodology for moving meshes in the QALE-FEM could also produce good quality of meshes in these cases. Some illustrations have been given for the cases with forced motions in Fig. 9. Apart from these, extensive investigations have also been made for the cases associated with free-response floating bodies during the development of the method. One case will be presented in this section to demonstrate the effectiveness of the method in producing good meshes at all time steps. The same floating body described in Section 7.2 is used, which is subjected to a wave with the height of 7 cm and the frequency parameter of $\xi = 0.65$ in a tank of $L = 10$. This case is run on a PC (Pentium IV 2.53 GHz processor, 1G RAM). The fluid domain is discretised into about 129,732 elements and 28,725 nodes.

Fig. 23 presents the mesh at different instances, where the right column illustrates the enlarged mesh in the vicinity of the body surface. Fig. 23a depicts the initial unstructured mesh while Figs. 23b and c show the meshes in the same area but after quite long time simulation. These figures demonstrate that the original refinement and distribution are maintained well and all elements are in satisfactory shape during the simulation. In addition, negative elements, which are of concern when using the linear spring analogy method, do not appear. Nevertheless, certain changes in the sizes and shapes of individual elements are observed and expected because the fluid domain varies with propagation of waves. It is these changes that make it possible to conform to the moving boundaries at all time steps and so to achieve satisfactory results as demonstrated in previous sections. In addition, the CPU time spent on moving the mesh at each time step is on average about 1 s, including 0.01 s for moving mesh on the body surface, approximately the same as the CPU time spent on sandbar problems in [1]. The CPU time spent on all calculations in one step is about 7 s on average. It indicates that the method used to move mesh in the QALE-FEM in cases with floating bodies is as efficient as in cases without floating bodies. It also indicates that useful results for a problem like these may be obtained in several hours by using a normal PC.

For cases with floating bodies, the ISITIMFB procedure for calculating forces has been developed in this paper. The accuracy and stability of the procedure have been investigated in Section 7.2.2. In this section, the efficiency of the procedure is discussed by comparing it with mode-decomposition method with the

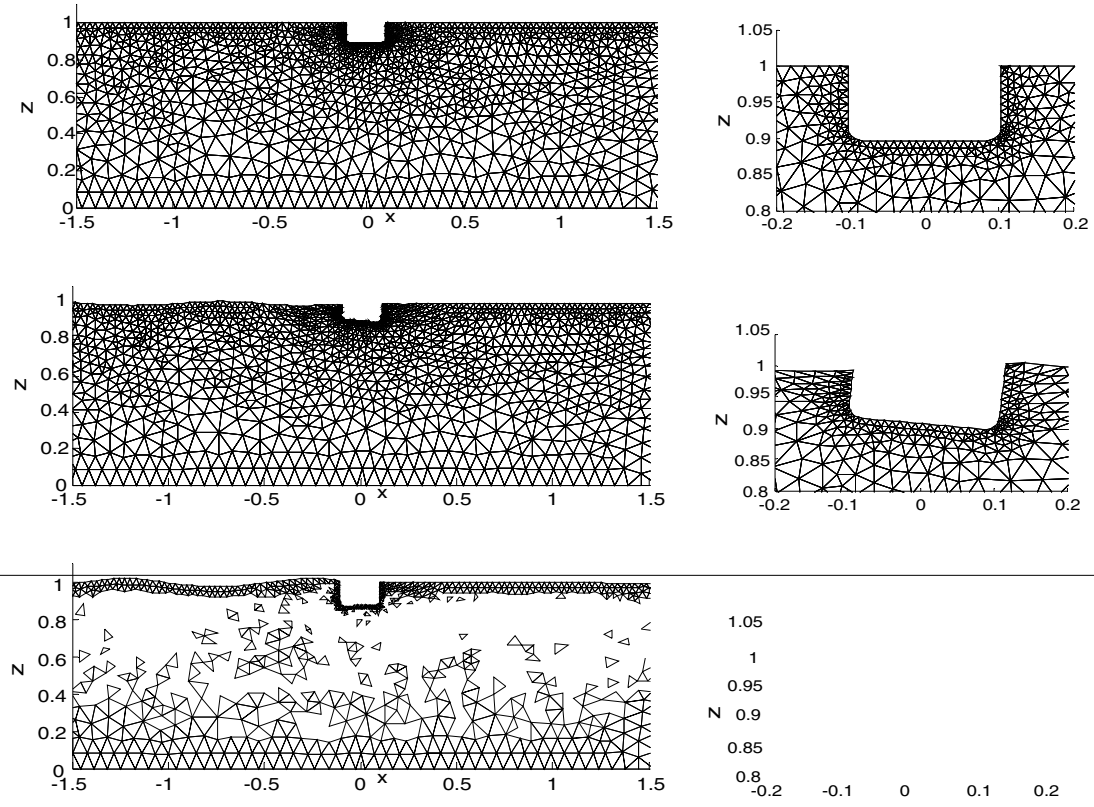

fourth-order Runge–Kutta method as the time integration scheme. In the later method, the motion is decomposed into 4 modes in 2D cases to find the solution for the potential derivatives ($\partial\phi/\partial t$) by solving 4 different boundary value problems in addition to one for the velocity potential (ϕ). Thus, total 5 different boundary value problems must be dealt with for one sub-step and therefore total 20 different boundary value problems for calculating ϕ and $\partial\phi/\partial t$ need to be solved in one time step forward. In addition, updating of the coefficient matrix is necessary to achieve stable solution as discussed in Section 7.2.2. On the other hand, when using our ISITIMFB, the number of iterations in one step forward is on average 7 for the case in Fig. 23 by using the control error of 1% in the procedure and so about 15 boundary value problems need to be solved without the necessity of updating the coefficient matrix. Therefore, for this case, the CPU time required by the ISITIMFB is less than 75% of that required by the mode-decomposition method. Although the CPU time used by the ISITIMFB is problem-dependent, it is more efficient as long as the number of iterations in the ISITIMFB is less than 10; this may not be exceeded in many cases unless choosing a control error and a time step that are unnecessary small, as indicated in Section 7.2.2. In addition, if the mode-decomposition method with the fourth-order Runge–Kutta scheme is used in our QALE-FEM method, the calculation of velocities on the free surface with unstructured meshes must be performed five times in one time step forward, which likely requires considerable more CPU time. Consequently, the ISITIMFB is a procedure that is efficient and is best matched with our QALE-FEM method.

9. Conclusion

In this paper, the QALE-FEM developed in our previous papers [1,2] is extended to simulate nonlinear interaction between water waves and 2D floating bodies based on the FNPT Model. In this method, the boundary value problems for the velocity potential and its time derivatives are solved by using a finite element

method; and the mesh is moved in order to conform to the variations of the free surface and the body surface by the spring analogy method specially proposed for these problems. The method allows the efficient use of unstructured mesh without the need to regenerate it at every time step, which is a necessary and very costly feature of the conventional FEM. The main developments in this paper are the techniques required for dealing with 2D nonlinear wave–body interactions. They include a scheme for moving mesh near and on the body surface, the ISITIMFB procedure for efficiently estimating the velocities and accelerations of bodies as well as the forces on them, the method for evaluating the fluid velocity on the surface of bodies and the use of wavemaker ramp functions and an artificial damping technique for shortening the transient period.

The newly extended method has been validated by comparing its numerical predictions of forces on bodies undergoing forced motions with analytical solutions. Comparison has also been made between the numerical results from this method for the RAOs of a free-response floating body and experimental data. Good agreement has been achieved in all the comparisons. Assessments are made on the efficiency of moving mesh and the quality of elements obtained by the QALE-FEM. These show that the unstructured mesh quality is satisfactorily maintained at all time steps even when the complex interactions between waves and free-response floating bodies are involved and also that the QALE-FEM requires a little time for moving mesh. Due to these developments, the useful results for a 2D floating body may be obtained in several hours using a normal PC.

Acknowledgements

This work is sponsored by EPSRC, UK (GR/R78701), for which the authors are most grateful. The authors are also grateful for the constructive comments and suggestions from two anonymous referees, which make the paper dramatically improved.

References

[1] Q.W. Ma, S. Yan, Quasi ALE finite element method for nonlinear water waves, J. Comput. Phys. 212 (2006) 52–72.
[2] S. Yan, Q.W. Ma, Application of QALE-FEM to the interaction between nonlinear water waves and periodic bars on the bottom, in: 20th International Workshop on Water Waves and Floating Bodies, Norway, 2005.
[3] C. Lachaume, B. Biausser, S.T. Grilli, P. Fraunie, S. Guignard, Modeling of breaking and post-breaking waves on slopes by coupling of BEM and VOF methods, in: Proceedings of the International Offshore and Polar Engineering Conference, 2003, pp. 1698–1704.
[4] G.F. Clauss, U. Steinhagen, Numerical simulation of nonlinear transient waves and its validation by laboratory data, in: Proceedings of the 9th International Offshore and Polar Engineering Conference, Brest, France, 1999, pp. 368–375.
[5] Q.W. Ma, G.X. Wu, R. Eatock Taylor, Finite element simulation of fully non-linear interaction between vertical cylinders and steep waves. Part 1: Methodology and numerical procedure, Int. J. Numer. Meth. Fluids 36 (2001) 265–285.
[6] Q.W. Ma, G.X. Wu, R. Eatock Taylor, Finite element simulation of fully non-linear interaction between vertical cylinders and steep waves. Part 2: Numerical results and validation, Int. J. Numer. Meth. Fluids 36 (2001) 287–308.
[7] M.S. Longuet-Higgins, E.D. Cokelet, The deformation of steep waves on water: I. A numerical method of computation, Proc. R. Soc. Lond. A 350 (1976) 1–26.
[8] T. Vinje, P. Brevig, Nonlinear ship motion, in: Proceedings of the 3rd International Conference on Numerical Ship Hydrodynamics, Paris, France, 1981, pp. 257–268.
[9] W.M. Lin, J.N. Newman, D.K. Yue, Nonlinear forced motion of floating bodies, in: Proceedings of the 15th Symposium on Naval Hydrology, Hamburg, Germany, 1984, pp. 33–49.
[10] P. Wang, Y. Yao, M. Tulin, An efficient numerical tank for nonlinear water waves, based on the multi-subdomain approach with BEM, Int. J. Numer. Meth. Fluids 20 (1995) 1315–1336.
[11] M. Kashiwagi, Full-nonlinear simulations of hydrodynamic forces on a heaving two-dimensional body, J. Soc. Nav. Archit. Jpn. 180 (1996) 373–381.
[12] Y. Cao, W.W. Schultz, R.F. Beck, Three-dimensional desingularised boundary integral method for potential problems, Int. J. Numer. Meth. Fluids 12 (1991) 785–803.
[13] M.S. Celebi, M.H. Kim, R.F. Beck, Fully nonlinear 3D numerical wave tank simulation, J. Ship Res. 42 (1998) 33–45.
[14] S.T. Grilli, P. Guyenne, F. Dias, A fully nonlinear model for three-dimensional overturning waves over arbitrary bottom, Int. J. Numer. Meth. Fluids 35 (2001) 829–867.
[15] M.H. Kim, M.S. Celebi, D.J. Kim, Fully nonlinear interactions of waves with a three-dimensional body in uniform currents, Appl. Ocean Res. 20 (1998) 309–321.
[16] G.X. Wu, R. Eatock Taylor, Finite element analysis of two dimensional non-linear transient water waves, Appl. Ocean Res. 16 (1994) 363–372.
[17] G.X. Wu, R. Eatock Taylor, Time stepping solution of the two dimensional non-linear wave radiation problem, Ocean Eng. 22 (1995) 785–798.

[18] Q.W. Ma, Numerical simulation of nonlinear interaction between structures and steep waves, Ph.D. Thesis, Department of Mechanical Engineering, University College, London, UK, 1998.
[19] Y. Cao, R.F. Beck, W.W. Schultz, Nonlinear computation of wave loads and motions of floating bodies in incident waves, in: 9th International Workshop on Water Waves and Floating Bodies, Kuju, Oita, Japan, 1994, pp. 33–37.
[20] K. Tanizawa, A nonlinear simulation method of 3-D body motions in waves (1st Report), J. Soc. Nav. Archit. Jpn. 178 (1995) 179–191.
[21] K. Tanizawa, M. Minami, On the accuracy of NWT for radiation and diffraction problem, in: The 6th Symposium on Nonlinear and Free-Surface Flow, 1998.
[22] K. Tanizawa, M. Minami, S. Naito, Estimation of wave drift force by numerical wave tank, in: Proceedings of the 9th ISOPE Conference, vol. 3, Brest, 1999.
[23] W. Koo, Fully nonlinear wave–body interactions by a 2D potential numerical wave tank, Ph.D. Thesis, Texas A&M University, 2003.
[24] W. Koo, M. Kim, Freely floating body simulation by a 2D fully nonlinear numerical wave tank, Ocean Eng. 31 (2004) 2011–2046.
[25] M. Kashiwagi, T. Momoda, M. Inada, A time-domain nonlinear simulation method for wave-induced motions of a floating body, J. Soc. Nav. Archit. Jpn. 84 (1998) 143–152.
[26] M. Kashiwagi, Nonlinear simulations of wave-induced motions of a floating body by means of the mixed Eulerian–Lagrangian method, Mech. Eng. 214 (2000) 841–855.
[27] G.X. Wu, Z.Z. Hu, Simulation of nonlinear interactions between waves and floating bodies through a finite-element-based numerical tank, Proc. A R. Soc. 460 (2004), No. 2050, 3037-3058.
[28] Q.W. Ma, M.H. Patel, On the nonlinear forces acting on a floating spar platform in ocean waves, Appl Ocean Res 23 (2001) 29–40.
[29] D. Sen, Numerical simulation of motions of two-dimensional floating bodies, J. Ship Res. 37 (4) (1993) 307–330.
[30] E.F.G. Dalen, Numerical and theoretical studies on water waves and floating bodies, Ph.D. Thesis, University of Twente, Enschede, 1993.
[31] K. Tanizawa, The state of the art on numerical wave tank, in: 4th Osaka Colloquium on Seakeeping Performance of Ships, Osaka, Japan, 2000, pp. 95–114.
[32] R. Eatock Taylor, B.T. Wang, G.X. Wu, On the transient analysis of the wavemaker, in: 9th International Workshop on Water Waves and Floating Bodies, Kuju, Oita, Japan, 1994.
[33] R. Eatock Taylor, Wave-maker ramp functions in numerical tanks, in: 20th International Workshop on Water Waves and Floating Bodies, Norway, 2005.
[34] P. Whittle, Prediction and Regulation by Linear Least-Square Methods, The English Universities Press Ltd., London, 1963.
[35] C. William Gear, Numerical Initial Value Problems in Ordinary Differential Equations, Prentice-Hall, Englewood Cliffs, NJ, 1971, pp. 102–115.
[36] O.M. Faltinsen, Sea Loads on Ships and Offshore Structures, Cambridge University press, United Kingdom, 1990.
[37] N. Nojiri, K. Murayama, A study on the drift force on two dimensional floating body in regular waves, Trans. West-Japan Soc. Nav. Arch. 51 (1975).